Structure Determination of Inactive-State GPCRs with a Universal Nanobody

Michael J. Robertson[1,2], Makaía Papasergi-Scott[1,2], Feng He[1,2], Alpay B. Seven[1,2], Justin G. Meyerowitz[1,2,3], Ouliana Panova[1,2], Maria-Claudia Peroto[1,2], Tao Che[4,5], Georgios Skiniotis[1,2,6]

[1]Department of Molecular and Cellular Physiology, Stanford University School of Medicine, Stanford, CA, USA

[2]Department of Structural Biology, Stanford University School of Medicine, Stanford, CA, USA

[3]Department of Anesthesiology, Perioperative and Pain Medicine, Stanford University School of Medicine, Stanford, CA 94305, USA

[4]Department of Anesthesiology, Washington University School of Medicine, St. Louis, Missouri, 63110, USA

[5]Center for Clinical Pharmacology, University of Health Sciences & Pharmacy at St. Louis and Washington University School of Medicine, St. Louis, Missouri, 63110, USA

[6]Correspondence: yiorgo@stanford.edu

Summary

Cryogenic electron microscopy (cryo-EM) has widened the field of structure-based drug discovery by allowing for routine determination of membrane protein structures previously intractable. However, despite representing one of the largest classes of therapeutic targets, most inactive-state G protein-coupled receptors (GPCRs) have remained

inaccessible for cryo-EM because their small size and membrane-embedded nature impedes projection alignment for high-resolution map reconstructions. Here we demonstrate that the same single-chain camelid antibody (nanobody) recognizing a grafted intracellular loop can be used to obtain cryo-EM structures of different inactive-state GPCRs at resolutions comparable or better than those obtained by X-ray crystallography. Using this approach, we obtained the structure of human neurotensin 1 receptor (NTSR1) bound to antagonist SR48692, of μ-opioid receptor (MOR) bound to the clinical antagonist alvimopan, as well as the structures of the previously uncharacterized somatostatin receptor 2 (SSTR2) in the apo state and histamine receptor 2 (H2R) bound to the antacid famotidine. Each of these structures yields novel insights into ligand binding and specificity. We expect this rapid, straightforward approach to facilitate the broad structural exploration of GPCR inactive states without the need for extensive engineering and crystallization.

Introduction

The impact of cryo-EM on structure-based drug discovery has been immense, leading to the characterization of a wide variety of new and valuable membrane protein drug targets, including ion channels and G protein-coupled receptors (GPCRs)[1]. As a key requirement for high-resolution cryo-EM map reconstructions, the randomly oriented particle projections must first be correctly aligned at intermediate-to-low resolution, a step that often fails for small proteins due to their limited structural features. For relatively small membrane proteins, the problem is compounded by the presence of a detergent micelle or lipid nanodisc used for solubilization, which further dampens the contrast of embedded

47 protein densities. These obstacles pose a major bottleneck for cryo-EM structure
48 determination of GCPRs, which account for roughly 35% of FDA-approved drugs.
49 Approximately half of those are agonists that activate the receptor and the other half
50 antagonists or inverse agonists[2] that engage the inactive-state receptor, thereby blocking
51 endogenous signaling. Active-state GPCR structures have been obtained by cryo-EM in
52 complex with heterotrimeric G protein[3], a ~90 kDa entity that adds significant mass
53 outside the detergent micelle or lipid disc and provides a source of alignment for the
54 transmembrane receptor. However, there is no such generalizable tool for cryo-EM
55 structure determination of inactive-state GPCRs, especially for family A receptors, the
56 largest GCPR subfamily with hundreds of receptors that are typically ~37-50 kDa and lack
57 sizeable extracellular domains for projection alignment. Thus, the application of cryo-EM
58 is severely limited for inactive-state GPCRs, and their structural elucidation mostly relies
59 on extensive engineering and crystallization trials for X-ray studies. This limitation impacts
60 mechanistic investigations of GPCRs and structure-based drug discovery for the
61 countless therapeutically relevant receptors.

62 Che *et al.*[4] recently reported a camelid VHH domain antibody, referred to as
63 nanobody 6 (Nb6), that engages the inactive-state intracellular loop 3 (ICL3) of the κ-
64 opioid receptor (KOR), even when this loop is grafted onto a wide range of receptors,
65 including orphan receptors and family B receptors. This tool was initially developed as a
66 bioluminescence resonance energy transfer (BRET)-based sensor of receptor activation
67 state, an approach that also allows for cost-effective and robust screening of Nb6-binding
68 constructs by employing BRET assays. Using the Nb6 approach, we obtained three-
69 dimensional (3D) map reconstructions of human NTSR1 (hNTSR1) in complex with Nb6

70 bound to the inverse agonist SR48692[5] at a resolution of 2.4 Å; the mouse MOR bound
71 to a megabody[6], an enlarged nanobody construct derived from Nb6 (Mb6), in complex
72 with the antagonist alvimopan[7] at a resolution of 2.8 Å; and the unliganded (apo) structure
73 of human SSTR2 bound to Nb6 at 3.1 Å resolution. Further, a modified Nb6 (Nb6M) was
74 cloned by grafting antigen-binding loops onto an alpaca nanobody scaffold and coupled
75 with a nanobody-binding antibody fragment (NabFab[8]) to determine the structure of
76 histamine receptor 2 (H2R) bound to famotidine at 3.0 Å resolution. Through these four
77 structures, we demonstrate that Nb6 is a general solution for determining high-resolution
78 inactive-state GPCRs by cryo-EM. Besides alleviating the need for extensive construct
79 engineering and crystallogenesis, the cryo-EM/Nb6 approach has two distinct
80 advantages: first, it does not necessitate the screening and development of receptor-
81 specific nanobodies. Second, the Nb6 BRET-based sensor allows for rapid and efficient
82 screening of constructs and conditions instead of time-consuming and expensive cryo-
83 EM-based screening.
84
85 **Employing Nb6 for cryo-EM structure determination of GPCRs**
86 Any fiducial marker used for cryo-EM structure determination of a target
87 macromolecule needs to be rigid in its binding and orientation in respect to the structural
88 target. Furthermore, if the marker is particularly small related to the target, it must be
89 positioned to provide a distinct feature from various angles to allow unambiguous
90 alignment of the randomly-oriented cryo-EM projections. A crystal structure of Nb6 bound
91 to KOR revealed an interaction at the base of TM5 and TM6, off-center from the major
92 axis of the receptor[4]. We hypothesized that this type of interaction would be an ideal

93 asymmetric fiduciary for cryo-EM particle projection alignment as it would allow for the
94 determination of the rotational orientation of the receptor around its major axis, particularly
95 during initial low-resolution alignments.

96 To evaluate the degree of rigidity of Nb6 when bound to a GPCR, we first
97 performed all-atom molecular dynamics (MD) simulations using the crystal structure of
98 the KOR-Nb6 complex. Alignment of the MD trajectories on the receptor atoms and
99 calculation of the average root mean squared fluctuation (RMSF) for Nb6 atoms over the
100 final 100 ns of triplicate 500 ns simulations (Fig. 1a) showed that Nb6 is rigidly bound and
101 characterized by little flexibility, except for the distal loops at the base of the nanobody.

102 Encouraged by these computational predictions, we employed Nb6 for *de novo*
103 cryo-EM structure determination of four pharmacologically relevant family A GPCRs. The
104 first, NTSR1, is broadly associated with neurological and gastrointestinal processes[9].
105 Overexpression of NTSR1 in some tumor types promotes cancer progression and
106 metastasis and is thus associated with poor prognosis[10], prompting the study and
107 development of NTSR1 inverse agonists for oncology[11]. We also studied MOR, the target
108 of opioids, which are both the most effective treatment for pain and also the therapeutic
109 class underlying the ongoing opioid epidemic in the United States[12]. While current opioid
110 antagonists can treat acute opioid overdose, there is an urgent need for MOR antagonists
111 with improved pharmacokinetic properties[12,13]. SSTR2 plays a pivotal role in the
112 neuroendocrine system by opposing the release of many hormones, including growth
113 hormone[14]. SSTR agonists are commonly prescribed for neuroendocrine tumors, while
114 SSTR subtype-selective antagonists are in development for diabetes, but the lack of
115 structural information for any somatostatin receptor family member in either active or

116 inactive state has made the development of next-generation SSTR ligands challenging.
117 Finally, selective H2R antagonists have a long history of clinical usage for peptic ulcers
118 and gastroesophageal reflux disease and are amongst the most prescribed drugs.
119 However, only structures of histamine receptor 1, the target for commonly prescribed
120 drugs for allergic rhinitis and other allergies, have been determined to date, impeding a
121 full understanding of histamine receptor subtype selectivity.

122 As originally described in Che *et al.*, we engineered constructs to enable binding
123 of Nb6 to mouse MOR and human SSTR2 by identifying minimal swaps of ICL3 along
124 with the cytoplasmic tips of transmembrane helix 5 and 6 (TM5/6) with that of the KOR
125 (Fig. 1c). In the case of the closely related MOR, the two point mutations M264L and
126 K269$^{6.24}$R (Ballesteros-Weinstein notation[15]; Fig. 1c) were sufficient to enable Nb6
127 binding. SSTR2 was able to bind Nb6 with the swap of all 15 residues from S238$^{5.68}$ of
128 TM5 (V256$^{5.68}$ of KOR) to K252$^{6.31}$ of TM6 (R270$^{6.31}$ of KOR) (Fig. 1c). For human NTSR1
129 (hNTSR1) we utilized the same swap from KOR T247$^{5.59}$ to L277$^{6.38}$ as previously
130 described for rat NTSR1[4] (rNTSR1; Fig. 1c). Similarly, for human H2R we used an
131 identical hybrid as described in Che *et al.* (KOR V244$^{5.56}$ to V285$^{6.46}$, Fig 1c). Notably,
132 BRET assays of agonist-induced Nb6 dissociation confirmed construct functionality, with
133 all four receptors showing dissociation of the nanobody in response to agonist binding
134 (Fig. 1d-g). In all experimental replicates, the BRET data for MOR response to DAMGO
135 appears to be biphasic, consistent with prior nanobody-based MOR activation sensors[16],
136 where distinct plasma membrane and endosomal signaling results in a two-phase
137 response.

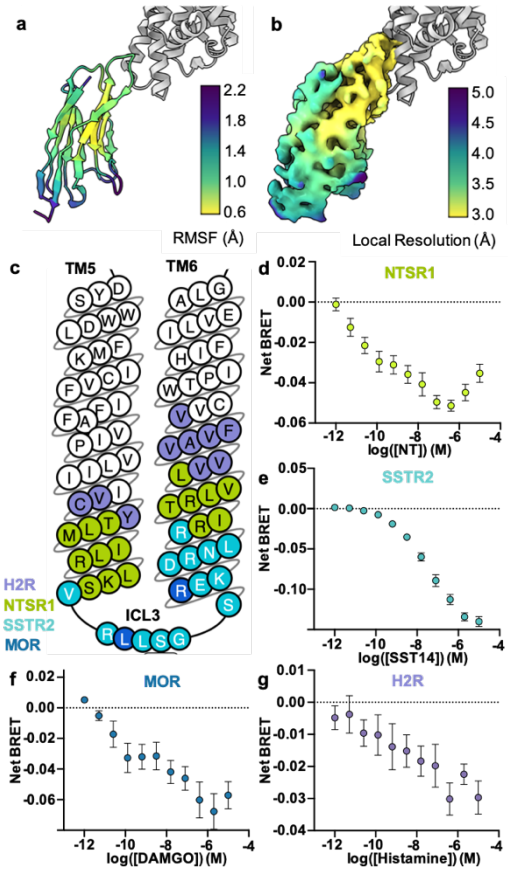

Fig 1. Construct design & evaluation for inactive state GPCR structure determination

a, Root mean squared fluctuations (RMSF) in atomic positions overaged over triplicate molecular dynamics simulations for Nb6 bound to KOR. **b,** local resolution plot of Nb6 from the SSTR2/Nb6 complex cryoEM map. **c,** overlay of the three KOR ICL3 constructs used to enable Nb6 binding for MOR (two point mutations), SSTR2 (5.68 to 6.31), and hNTSR1 (5.59 to 6.38). Dose-response curves representing loss of BRET transfer (net BRET) between Receptor-rLuc and Nb6-mVenus for **d,** $NTSR1_K$ and neurotensin (NT), **e,** MOR_K and DAMGO, **f,** $SSTR2_K$ and SST14, and **g,** $H2R_K$ and histamine.

High-resolution cryo-EM structure determination was feasible in all cases. Despite Nb6 being only 12 kDa, Nb6, or the equivalent region of Mb6, is resolved in three maps, providing a critical stable density outside the detergent micelle surrounding NSTR1, MOR and SSTR2. Notably, the local resolution indications for Nb6 in our GPCR/Nb6 complex cryo-EM maps showed a high correlation with the relative root mean square fluctuation (RMSF) values for Nb6 calculated from our MD simulations (Fig. 1c). This observation further demonstrates the strong predictive power of MD simulations in assessing the behavior of fiducial markers for such work. In the case of H2R/Nb6M/NabFab, the entire complex is fairly rigid and well resolved, due, in part, to the nanobody modifications and/or the binding of the NabFab rigidifying the loops of Nb6M.

149 **Structure of hNTSR1**

150 Obtaining inactive-state crystal structures has proven challenging for NTSR1. The

151 only available crystal structures were determined in 2021[17]: one with a receptor in the apo

152 state (3.19 Å) and several structures with the receptor bound to the inverse agonists

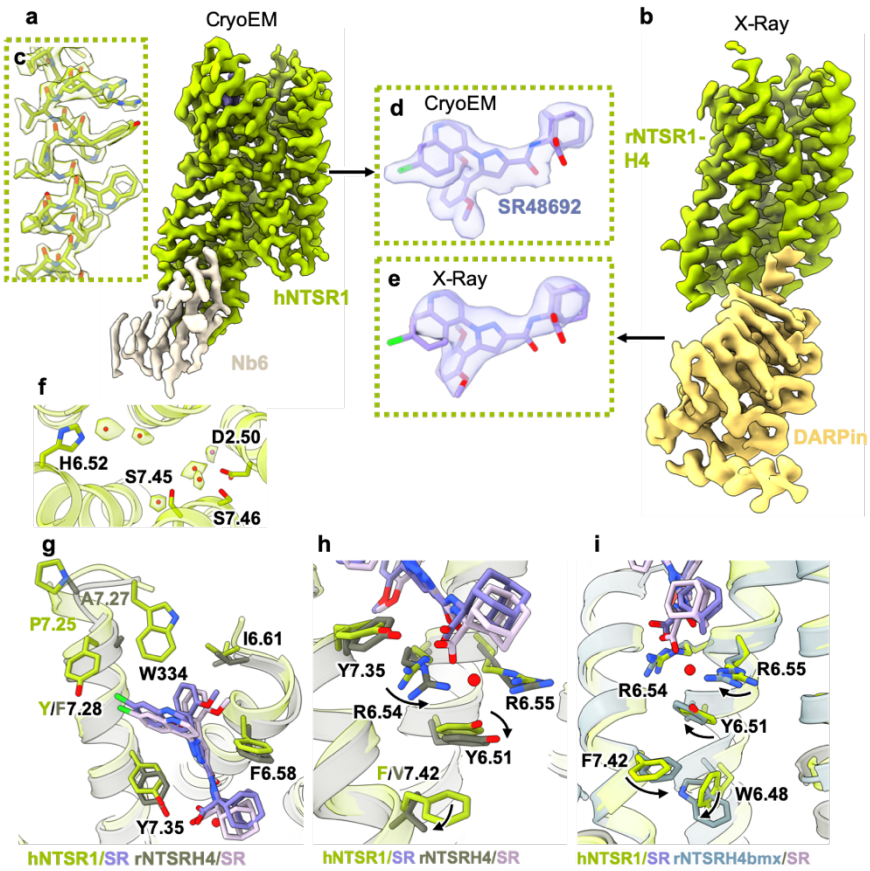

Fig 2. Comparison of cryoEM structure of hNTSR1 and crystal structure of rNTSR1-H4 and rNTSR1-H4bmx

a, 2.4 Å global resolution cryoEM map of hNTSR1. **b,** 2Fo-Fc crystallography map at 2.6 Å of rNTSR-H4 contoured at σ=1.0. **c,** hNTSR1 TM5 with cryoEM map **d,** Local EM map around bound inverse agonist SR48692. **e,** Local 2Fo-Fc map around SR48692 contoured at σ=1.25. **f,** Waters resolved in the core of the hNTSR1 receptor overlaid with the cryoEM map. **g,** Overlay of the hNTSR cryoEM structure (protein in green, SR48692 in purple) with the rNSTR-H4 crystal structure (protein in gray, SR48692 in pink) highlighting differences in ECL2. **h,** Overlay of the hNTSR cryoEM structure (protein in green, SR48692 in purple) with the rNSTR-H4 crystal structure (protein in gray, SR48692 in pink) highlighting the residue shift and probable loss of bound water molecule caused by the F7.42V thermostabilizing mutation **i,** Overlay of the hNTSR cryoEM structure (protein in green, SR48692 in purple) with the rNSTR-H4bmx crystal structure (protein in gray, SR48692 in pink)

153 SR48692 (2.64 Å, 2.70 Å) or SR142948A (2.92 Å), which are small molecules previously
154 in development for treating cancer. Obtaining these structures required extensive
155 engineering to facilitate protein crystallization, with that work employing a construct of rat
156 NTSR1 evolved in bacteria to acquire numerous thermostabilizing mutations and fused
157 in TM7 with a DARPin[18] protein domain to facilitate crystal packing (rNTSR1-H4),
158 although a structure was also obtained with a back-mutated construct (rNTSR1-H4bmx)
159 at several positions to attempt to visualize a more native state[19]. To assess and compare
160 the cryo-EM/Nb6 approach with crystallography we obtained the cryo-EM structure of
161 hNTSR1/Nb6 complex bound to SR48692 (Fig. 2a, Extended Data Fig. 2). Notably, the
162 cryo-EM structure was resolved at a global resolution of 2.4 Å, both a higher nominal
163 resolution than the crystal structure and with better-resolved features, including the
164 density corresponding to the ligand (Fig. 2a-e, Extended Data Fig. 3a, 3b, 8a). This
165 resolution range also reveals densities corresponding to extensive hydration throughout
166 the receptor in the cryo-EM map (Fig. 2f, Extended Data Fig. 3c).

167 The construct for hNTSR1 was minimally modified beyond the KOR ICL3 swap,
168 with only N- and C- termini truncations in regions not resolved in typical family A structures
169 and a single A85$^{1.54}$L mutation to increase expression[20]. While the general ligand pose is
170 very similar, the cryo-EM structure reveals additional interactions not observed in the
171 rNTSR-H4 and/or rNTSR-H4bmx crystal structures. First, remodeling of the TM7-ECL3
172 region allows W334 in ECL3 to be fully resolved in the hNTSR1 structure loosely capping
173 the top of the hydrophobic chloro-naphthyl and dimethoxy-phenyl moieties of SR48692
174 (Fig. 2g). This change may be due to several amino acid sequence differences at the top
175 of TM7, most prominently P336$^{7.25}$ in hNTSR1 versus T341$^{7.25}$ in rNTSR1, with the proline

176 inducing a sharp turn between the top of TM7 and ECL3 in hNTSR1. In addition, a
177 rearrangement of R327$^{6.54}$ in rNTSR-H4 (R322$^{6.54}$ in hNTSR1) appears to disrupt a water-
178 mediated interaction between R327$^{6.54}$, R328$^{6.55}$ (R323$^{6.55}$ in hNTSR1), and the
179 carboxylate moiety of SR48692 observed in the hNTSR1 structure (Fig. 2h). This R327$^{6.54}$
180 rearrangement likely stems from the F358$^{7.42}$V thermostabilizing mutation in rNTSR-H4,
181 allowing a downward relaxation of Y324$^{6.51}$ (Y319$^{6.51}$ in hNTSR1) and R327$^{6.54}$. This water
182 molecule is also displaced in the rNTSR-H4bmx structure due to a different
183 rearrangement of R327$^{6.54}$ and R328$^{6.55}$, likely resulting from a shift in the W321$^{6.48}$
184 rotamer not observed in either hNTSR1 or rNTSR-H4bmx (Fig 2i). Notable differences
185 also exist in the TM helices between the two structures; TM1 is shifted with respect to the
186 core of the receptor in both crystal structures in varying degrees and directions (Extended
187 Data Fig. 3d). In addition, the top of TM2 and ECL1 are out of register by one residue
188 between hNTSR1 and rNTSR-H4. While this may be due to the differences in
189 experimental constructs, the observed discrepancy may also result from the fact that even
190 at σ=1 the 2Fo-Fc map of the crystal structure lacks sidechain information in the ECL1
191 region, rendering modeling ambiguous (Extended Data Fig. 3e,f). Overall, the lack of
192 thermostabilizing mutations and DARPin in TM7 restores a more native-like inactive state
193 as suggested by the conformation of key amino acids. For example, Y364$^{7.53}$ of the
194 hNTSR1 NPxxY motif (Y369$^{7.53}$ in rNSTR1) occupies a position and rotamer more typical
195 of an inactive state family A GPCR (Extended Data Fig. 3g).
196
197 **Structure of MOR**

198 Using the same approach, we obtained a cryo-EM structure of the MOR bound to
199 the non-blood brain barrier penetrant, MOR selective inverse agonist alvimopan, an FDA-
200 approved drug for reversing opioid-induced gastrointestinal (GI) symptoms in hospital
201 settings. In the case of NTSR1/Nb6, vitrifying the sample in a very thin buffer layer on
202 holey gold grids[21] was necessary for high resolution and to achieve proper alignment of
203 particle projections. To assess an alternative approach, we used Nb6 to develop a
204 megabody, termed 'Mb6', a fusion of a nanobody and a scaffold protein of either 45 or 86
205 kDa that can serve as a larger fiducial marker, based on the work of Uchański *et al.*[6]. In
206 that work, the Mb designs employed for $GABA_A$ and WbaP resulted in cryo-EM maps that
207 could not resolve well past the nanobody portion, presumably due to flexibility. We thus
208 opted instead for using the c7HopQA12 design, which incorporates a twisted linker
209 between the nanobody and the 45 kDa HopQ scaffold to increase their contact and,
210 ideally, rigidity. However, our MD simulations suggested that even this design was
211 characterized by substantial flexibility between the Nb and scaffold (Extended Data Fig.
212 5a). In agreement with this result, our cryo-EM 2D class averages of the MOR-Mb6
213 complex showed that only the Nb6-receptor portion is well resolved, with the scaffold
214 averaging out (Extended Data Fig. 4b). Nevertheless, leveraging the ordered Nb6 portion
215 of Mb6 in our cryo-EM data, we obtained a 2.8 Å cryo-EM map (Fig. 3a, Extended Data
216 Fig. 4) with unambiguous density for the ligand and receptor (Fig. 3c, Extended Data Fig.
217 8b). This level of detail is quite comparable to the 2.8 Å crystal structure of MOR (Fig. 3b,
218 d), although the cryo-EM map further resolves several probable water molecules in the
219 ligand binding site, including one that bridges interactions between the carboxylate of
220 alvimopan and the receptor (Extended Data Fig. 5b).

221 Comparing the binding poses of the MOR-selective alvimopan with that of the
222 structurally similar ligand JDTic, which is selective for KOR, reveals a striking difference.
223 Despite their similar scaffolds, the phenol-piperidine moieties of alvimopan and JDTic are
224 in completely different positions and orientations, nearly flipped in the binding pocket.
225 Aligning our structure with KOR-JDTic (PDB:4DJH[22]) reveals that JDTic would clash with
226 Y326$^{7.43}$ and Q124$^{2.60}$ in MOR, while alvimopan would clash with W124 and I294$^{6.55}$ in

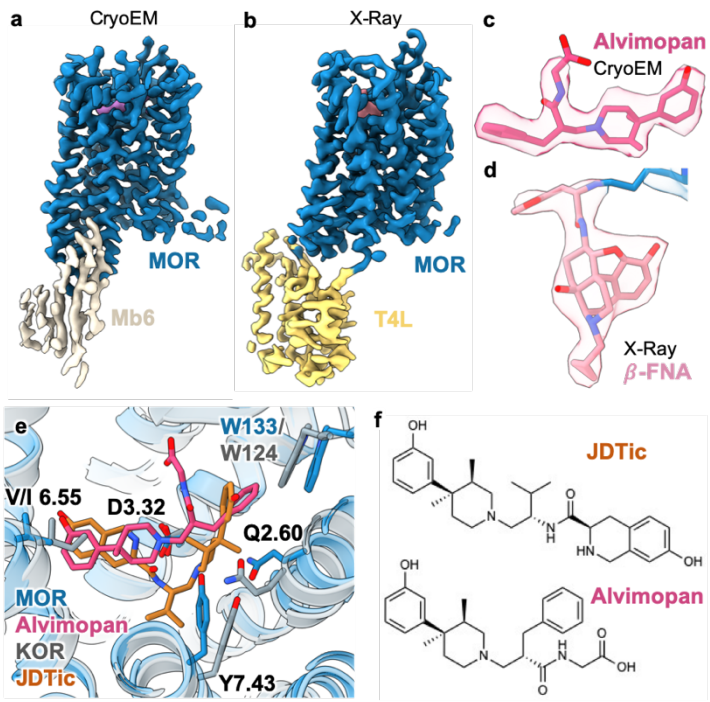

Fig 3. Comparison of cryo-EM structure of alvimopan-bound MOR with crystal structures of MOR/β-FNA and KOR/JDTic
a, Cryo-EM map of MOR at 2.8 Å global resolution. **b,** 2Fo-Fc crystallography map of MOR at 2.8 Å contoured at σ=2.0. **c,** Cryo-EM density and model for inverse agonist alvimopan. **d,** Local 2Fo-Fc map around β-FNA contoured at σ=1.5. **e,** overlay of the alvimopan pose in the MOR cryo-EM structure (protein in blue, alvimopan in magenta) with the JDTic pose in the KOR crystal structure (protein in grey, JDTic in orange). **f,** Comparison of JDTic and alvimopan chemical structures highlighting similar phenol-piperidine scaffold.

227 KOR (I294$^{6.55}$ of KOR is substituted by a repositioned valine in MOR). In addition to the
228 steric confines of the binding pocket, charge differences also appear to contribute to the
229 differences in binding pose between JDTIC and alvimopan. The nitrogen of the
230 tetrahydroisoquinoline ring system of JDTic is likely also protonated or perhaps
231 protonated instead of the piperidine, and thus forms salt bridge interactions with D138$^{3.32}$
232 (D147$^{3.32}$ in MOR), just as the protonated piperidine of alvimopan does in MOR. Of note,
233 alvimopan shares similarities to fentanyl and its analogues, including a central piperidine

234 ring. Computational docking of carfentanil[23], a potent MOR agonist, in the active-state
235 structure of the receptor[3] suggests a pose similar to alvimopan, but with the additional
236 phenylamine moiety on the piperidine ring positioned to bind into the pocket occupied by
237 the toggle switch tryptophan W293$^{6.48}$ (Extended Data Fig. 5a). How a MOR ligand
238 engages this region is often the main determining factor for its agonism versus
239 antagonism. Based on our observations, we hypothesize that this phenyl moiety of
240 fentanyl and its derivatives is responsible for converting the piperidine scaffold to an
241 agonist.
242
243 **Structure of SSTR2**
244 To test the cryo-EM/Nb6 approach on a receptor without prior structural
245 characterization we chose SSTR2, a member of the SSTR subfamily for which no
246 structures have been determined. Despite the absence of a stabilizing inverse agonist or
247 any other ligand, and not using an energy filter for cryo-EM data acquisition (typically
248 beneficial for improved contrast when imaging small proteins), we were able to obtain a
249 3.1 Å map of SSTR2/Nb6 with well-resolved features (Fig. 4a, Extended Data Fig. 6, 8c).
250 Together with two active-state structures of SSTR2 bound to two different agonists, the
251 endogenous 14-mer SST14 and the synthetic 8-mer octreotide[24], the inactive-state
252 SSTR2 structure enabled us to characterize several aspects of receptor activation and
253 ligand recognition. Perhaps the most interesting feature of SSTR2 is the conformational
254 flexibility of ECL2; while in a well-defined position in the apo state structure, ECL2 is
255 pushed to a more open conformation when bound to the endogenous agonist SST14, but
256 folds down over the top of the receptor in the octreotide-bound state (Fig. 4b). As a

consequence of the ECL2 plasticity, different residues are engaged in binding the pan-SSTR agonist SST14 versus the SSTR2-selective octreotide. This is an important factor to SSTR subtype selectivity, which is explored further in our recent study[24].

Very few structures have been obtained to date for family A GPCRs in the unliganded, apo state, primarily due to the general need for a stabilizing ligand to obtain a crystal structure. Experimentally-derived apo structures provide an opportunity to

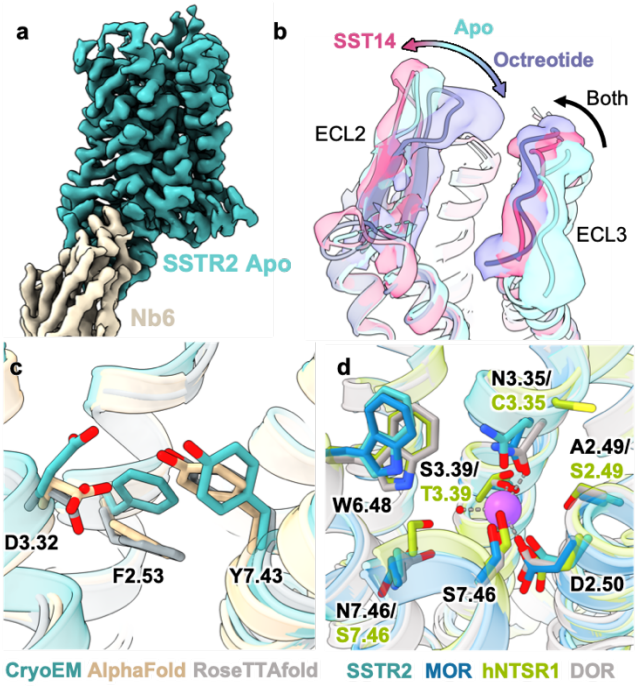

Fig 4. | Cryo-EM structure of the apo SSTR2 and comparison of sodium ion binding site.
a, Cryo-EM map of SSTR2 at 3.1 Å global resolution. **b,** Comparison of the model and cryo-EM maps of apo SSTR2 (teal) and SSTR2 in complex with either SST14 (magenta) or octreotide (purple). **c,** Comparison of the CryoEM structure of SSTR2 (teal) with AlphaFold (tan) and RoseTTAfold (gray) predictions. **d,** Overlay of SSTR2 (teal), MOR (blue), and NTSR1 (green) cryo-EM structures around the canonical family A sodium ion binding site with the DOR sodium coordination site structure (gray, PDB:4N6H).

evaluate predicted structures from the recently published deep-learning based tools, AlphaFold2[25] and RoseTTAfold[26]. Notably, while both software performed well in predicting the overall structure of SSTR2, key details of the ligand binding site were in disagreement with the experimental structure, particularly in residues D122$^{3.32}$, F92$^{2.53}$, and Y302$^{7.43}$ (Fig. 4c), which are involved in ligand binding and activation, as detailed in the companion active-state SSTR2 manuscript[24]. Although a more systematic comparison is needed, this observation underscores both the merits and the potential limitations of homology model-based approaches. Differences in side chain positioning,

271 especially within a ligand binding site, can throw off structure-based drug discovery efforts
272 and other pursuits requiring high-accuracy coordinates.
273
274 **Differential sodium accommodation by family A GPCRs**
275 Our near-native inactive-state cryo-EM maps provide the opportunity to examine
276 the allosteric sodium binding site found deep in the core of many family A receptors. For
277 NTSR1, MOR, and SSTR2 there is strong experimental evidence for negative allosteric
278 modulation by sodium[27–29]. In both MOR and SSTR2, the identities of the residues in the
279 sodium binding site are the same as the δ-opioid receptor (DOR), for which there is a
280 high-resolution crystal structure (1.8 Å) with a well-defined sodium site[30] (Fig. 4c). The
281 geometries of the MOR, SSTR2, and DOR sites are very similar, with the exception of a
282 slight rearrangement of $W^{6.48}$ in the case of both MOR ($W293^{6.48}$) and SSTR2 ($W269^{6.48}$),
283 and $N125^{3.35}$ in SSTR2. In contrast to SSTR2 and MOR, hNTSR1 has four amino acid
284 differences in the sodium binding site, namely $T155^{3.39}$ (in place of $S^{3.39}$), $S357^{7.46}$ (in
285 place of $N^{7.46}$), $S111^{2.49}$ (in place of $A^{2.49}$), and $C151^{3.35}$ (in place of $N^{3.35}$). In the DOR
286 structure, both $S135^{3.39}$ and $N131^{3.35}$ directly interact with the sodium.
287 The three maps we determined resolve features consistent with water and/or ions
288 in the canonical sodium binding region near $D^{2.50}$, although only NTSR1 has sufficiently
289 high resolution in this region to facilitate unambiguous ion modeling (Extended Data Fig.
290 7a-c). The probable ion sites of SSTR2 and MOR match relatively well to those observed
291 in DOR. In the hNTSR1 map, we observe a density with close proximity to oxygen atoms
292 of $T155^{3.39}$, $S111^{2.49}$, $D112^{2.50}$ (Extended Data Fig. 7a). Even though precise identification
293 of water versus ion is challenging in cryo-EM maps, we expect that this feature

294 corresponds to the sodium, shifted by 1.8 Å compared to the sodium in DOR (Fig. 4d,
295 Extended Data Fig. 7d, e). As other receptors with resolved sodium ion sites have
296 cysteine or other hydrophobic residues in place of $N^{3.35}$, $S111^{2.49}$ is likely responsible for
297 the shift in sodium position in NTSR1. Overall, we find substantial similarity between the
298 sodium binding sites of inactive state GPCRs from cryo-EM and crystallography.
299
300 **Structural Basis of Histamine Receptor Subtype Selectivity**
301 Notwithstanding the success of Nb6 alone to obtain these structures, we sought to
302 generate a larger, rigid Nb6-based fiducial that would enable the alignment of potentially
303 more challenging targets and also extend this approach to less powerful electron
304 microscopy platforms. To this end we generated an 'alpacaized' Nb6 where the antigen
305 binding loops of Nb6 were grafted onto an alpaca nanobody scaffold[8]. This modified Nb6,
306 called Nb6M, was used to bind H2R possessing the KOR ICL3 swap in complex with the
307 FDA approved antacid drug famotidine. The complex was additionally decorated with a
308 NabFab[8] (a Fab antibody fragment that binds alpaca nanobodies) and an anti-Fab
309 nanobody that has been shown to reduce Fab flexibility[31]. The structure of the entire
310 complex was determined by cryo-EM at a global nominal resolution of 3.0 Å (Fig. 5a,
311 Extended Data Fig. 8). With the exception of the anti-Fab nanobody, the structure is well
312 resolved, with local refinement on the receptor and Nb6M region further enhancing the
313 details of H2R and bound famotidine (Fig. 5b, Extended Data Fig. 8e). Notably, a lipid
314 molecule can be observed wedged between TM1 and TM7 and interacting with $Q79^{2.62}$,
315 in a similar position observed previously in cryoEM maps with certain family A GPCRs[32]
316 although its role remains unclear (Extended Data Fig. 9a).

Comparing our cryo-EM structure of H2R/famotidine with the crystal structure of H1R bound to the H1R selective doxepin (PDB:3RZE[33]) reveals clearly the structural basis for subtype selectivity between H1R and H2R. H1R ligands, including the FDA approved doxepin, loratadine, and cetirizine (Extended Data Fig. 9b-d) possess a distinct diphenyl group that occupies a large hydrophobic pocket in H1R comprised of $W^{4.56}$, $F^{6.55}$, $F^{6.52}$, and $Y^{3.33}$ (Fig. 5c). These compounds also include a single amine which is protonated at neutral pH and interacts with the key aminergic aspartate $D^{3.32}$ present in many family A GPCRs. The hydrophobic pocket where the diphenyl moiety binds in H1R is substantially perturbed in H2R, with the substitution of $Y^{3.33}V$ and repositioning of $W^{4.56}$ in H1R with $S^{4.57}$ in H2R removing major hydrophobic and pi-pi interaction partners (Fig. 5c). Further, TM6 shifts inward, repositioning $F^{6.55}$ and $F^{6.52}$ and resulting in a partial closure of the pocket (Fig. 5c). Several additional residues, including $C^{3.36}$ ($S^{3.36}$ in H1R) occupy rotamers in the famotidine-bound state that would sterically clash with doxepin binding.

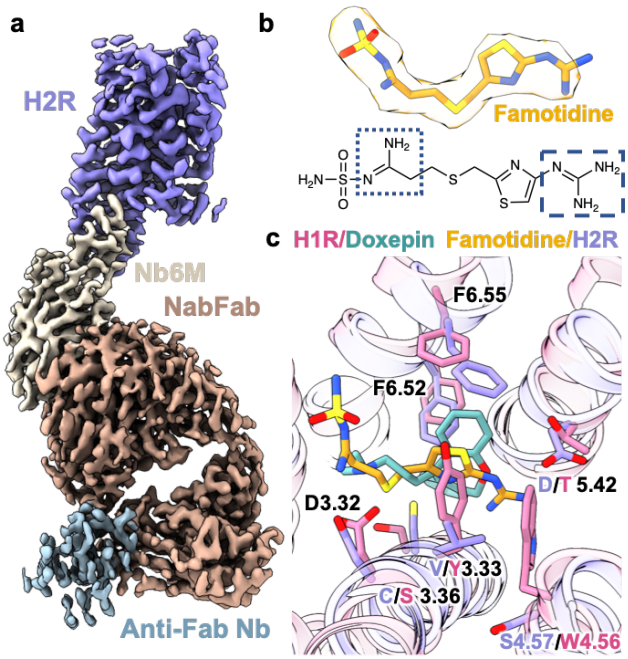

Fig 5. Cryo-EM structure of the H2R/Famotidine/Nb6M/NabFab/Anti-Fab complex and comparison to H1R/Doxepin

a, 3.0 Å global resolution cryo-EM map of inactive-state H2R complex. **b,** Famotidine in the cryo-EM density and chemical schematic; protonatable amine groups are boxed in blue, with the moiety protonated near neutral pH on the right in large dashed lines, and the moiety likely protonated at low pH on the left in small dotted lines. **c,** Overlay of H1R (magenta) and doxepin (teal) crystal structure with the H2R (lavender) and famotidine (gold) cryo-EM structure.

331 Famotidine and doxepin differ in their chemical structures, where famotidine is a
332 primarily linear molecule with two amine-containing moieties (Fig. 5b), a common feature
333 of H2R blockers (Extended Data Fig. 9e-g). These two amine-containing groups of H2R
334 antagonists tend to differ substantially in their pKas, with one that is likely protonated at
335 or near pH 7.0 (the guanidine group in the case of famotidine, Fig. 5b; dashed lines) and
336 a second that would require a far lower pH for protonation (the amidine/thiazole region
337 for famotidine[34], Fig. 5b, dotted lines). However, as H2R antagonists are primarily used
338 for diseases of gastric acid and bind to hydrochloric acid-secreting parietal cells, the
339 precise protonation state in the therapeutic environment is difficult to predict. Regardless
340 of protonation state, the binding pose is likely very similar; the protonated high-pKa amine
341 moiety forms a salt bridge with $D^{5.42}$ while the other amine-containing group interacts with
342 $D^{3.32}$ via either hydrogen bonding or a salt bridge (Fig. 5c). Prior functional studies have
343 also suggested that $D^{5.42}$ is a main determinant in subtype selectivity for H2R blockers[35],
344 with this position corresponding to a threonine in H1R, which is unable to form the key
345 salt bridge. Our docking studies with the other FDA approved H2R blockers cimetidine
346 and ranitidine suggest this 'di-aminergic' ligand binding at H2R is a common feature of
347 H2R antagonists (Extended Data Fig. 9e-g). Additional factors contributing to the lack of
348 binding of famotidine to H1R include the steric clash with $W^{4.54}$ (S in H2R) and the
349 modulation of the shape of the hydrophobic binding pocket (Fig. 5c).
350

351 **Discussion**

352 Here, we present inactive-state structures of four family A GPCRs, all obtained by
353 cryo-EM at resolutions as high as 2.4 Å by employing minimal engineering and a universal

354 nanobody for projection alignment. By using molecular dynamics simulations to assess
355 fiducial markers for use in cryo-EM structure determination, we could accurately predict
356 that Nb6 is sufficiently rigid for cryo-EM particle alignment, while Mb6 is too flexible for
357 resolution beyond the nanobody portion. Additionally, the enhanced decoration
358 opportunities afforded by the alpacaized Nb6M provide an additional tool for structure
359 determination of potentially more challenging targets and with less powerful cryo-EM
360 imaging set-ups such as those of 200kV and even 100kV. Each of the cryo-EM structures
361 described here yields new insights into ligand recognition, with resolution that is as good
362 or better than that of analogous structures produced by X-ray crystallography. In contrast
363 to active state GPCR-G protein complexes, where the highest-resolution portion of the
364 map is on the larger G protein due to the center of alignment, the inactive-state Nb6
365 GPCR structures display their highest resolution at the receptor core, facilitating accurate
366 modeling of ligands and their surrounding hydration. Even with the inclusion of NabFab,
367 local refinement on the receptor-Nb6M yielded a very well resolved ligand binding cavity.
368 This generalizable approach opens this broad family of drug targets to rapid,
369 crystallization-free structure determination, with biochemical stability of the receptor and
370 nanobody binding being the only limitations. As such, we anticipate Nb6 to be a broadly
371 applicable approach to determining inactive state structures of near-native GPCRs,
372 further propelling drug discovery in this class of receptors.
373

374 **Author Contributions**

375 M.J.R. cloned constructs, expressed and purified proteins, processed EM data, built
376 models, and ran/analyzed molecular dynamics simulations. M.P.S. expressed and

purified proteins and collected cryo-EM data. F.H. cloned constructs and expressed proteins. J.M. performed BRET assays. A.S. prepared cryo-EM samples and collected cryo-EM data. M.C. expressed proteins and purified nanobody. O.P. prepared cryo-EM samples and collected cryo-EM data. T.C. provided constructs for nanobody expression and BRET assays. M.J.R. and G.S. wrote the manuscript with input from M.P.S., F.H., J.M., O.P., and T.C.. G.S. supervised the project.

Data Availability

All data generated or analyzed in this study are included in this article and the Supplementary Information. The cryo-EM density maps and corresponding coordinates have been deposited in the Electron Microscopy Data Bank (EMDB) and the Protein Data Bank (PDB), respectively, under the following accession codes: NTSR1 (EMD-26589, PDB:7UL2), H2R (EMD-26590, PDB:7UL3), MOR (EMD-26591, PDB:7UL4), SSTR2 (EMD-26592, PDB:7UL5). Raw data has been deposited in EMPIAR under the following accession codes:

Competing Interests

The authors declare no competing interests.

Acknowledgements

We thank the Kobilka lab for providing plasmids of NTSR1 and MOR. We thank the Kossiakoff lab for providing the plasmid for NabFab and constructive feedback. Cryo-EM data were collected at the Stanford cryo-EM center (cEMc) with support from E.

Montabana. This work was supported, in part, by the Mathers Foundation (G.S.), training grant T32GM089626 (J.G.M.), the National Institute of Health R35GM143061 (T.C.), and used the Extreme Science and Engineering Discovery Environment (XSEDE)[36] resource comet-gpu through sdsc-comet allocation TG-MCB190153 (G.S.), which is supported by National Science Foundation grant number ACI-1548562.

Methods

Cloning

The cDNA for SSTR2 was obtained from Horizon Discovery and cloned into a pFastBac vector containing an N-terminal haemagglutinin (HA) signal sequence followed by a FLAG epitope (DYKDDDD) and a C-terminal C3 protease cleavage site followed by enhanced green fluorescent protein (eGFP) and a hexahistidine (His6) tag using Gibson cloning. Constructs for hNTSR1 and MOR were obtained from the lab of Brian Kobilka and have been described previously[3,20]. Briefly, each is cloned in pFastBac with an N-terminal haemagglutinin (HA) signal sequence followed by a Flag epitope (DYKDDDD) and a C-terminal HRV 3C protease cleavage site followed by a hexahistidine (His6) tag. In the case of hNTSR1, the His6 tag is preceded by enhanced green fluorescent protein (eGFP). For MOR, two point mutations (M264L and K269R) were introduced with site-directed mutagenesis; all PCR reactions were conducted with Q5 polymerase.

For hNTSR1, residues between T247$^{5.59}$ to L277$^{6.3}$ of kappa opioid were substituted,

421 for SSTR2, residues between S238 and K252 were replaced with those of kappa opioid
422 receptor, and for H2R residues from V244$^{5.56}$ to V285$^{6.46}$ were exchanged for kappa
423 opioid.

424 **Biolumescence resonance energy transfer (BRET) assays**

425 BRET assays were performed and analyzed as previously described[4] with the following
426 modifications: HEK-293S cells grown in FreeStyle 293 suspension media (Thermo
427 Fisher) were transfected at a density of 1 million cells/mL in 2 mL volume using 600 ng
428 total DNA at 1:1 ratio of Receptor-rLuc:Nb6-mVenus and a DNA:PEI ratio of 1:5,
429 and incubated in a 24 deep well plate at 220 rpm, 37°C for 48 hours. Cells were harvested
430 by centrifugation, washed with Hank's Balanced Salt Solution (HBSS) without
431 Calcium/Magnesium (Gibco), and resuspended in assay buffer (HBSS with 20 mM
432 HEPES pH 7.45) with 1 µg/mL freshly prepared coelenterazine h (Promega). Cells were
433 plated in white-walled, white-bottom 96 well plates (Costar) in a volume of 60 µl/well and
434 60,000 cells/well. Ligands were prepared in drug buffer (assay buffer with 0.1% BSA, 6
435 mM $CaCl_2$, 6 mM $MgCl_2$), and added at a 1:2 ratio of drug:cell suspension. Ten minutes
436 after the addition of ligand, plates were read using a SpectraMax iD5 plate reader using
437 485 nm and 535 nm emission filters with a one-second integration time per well. The
438 computed BRET ratios (mVenus/RLuc emission) were normalized to ligand-free control
439 (Net BRET) prior to further analysis.

440

441 **Expression and Purification of Nb6, Mb6, and Nb6M**

442 Wk6 *E. coli* (ATCC) were transformed via heat shock with Nb6 plasmid[4] and two 5 mL
443 starter cultures were grown overnight in LB supplemented with 100 µg/ml ampicillin. 2L

444 of terrific broth were supplemented with 100 μg/ml ampicillin, inoculated with starter
445 cultures, and grown at 37°C with shaking until OD_{600}=0.7. Expression was then induced
446 with 1mM IPTG and expression was allowed to proceed at 28°C overnight. Pellets were
447 harvested via centrifugation and washed once with phosphate-buffered saline before
448 snap freezing in liquid nitrogen. Pellets containing Nb6 were thawed and resuspended in
449 50 mM Tris pH 8.0, 0.5 mM EDTA, 20% w/v sucrose (TES) buffer at 15 mL / 1 liter pellet
450 and supplemented with protease inhibitor cocktail and shaken in an orbital shaker for 1
451 hour at 4°C. An additional 30 mL per 1 liter pellet of TES diluted 1:4 with water was added
452 and placed in an orbital shaker for an additional 45 minutes at 4°C. Cell debris was
453 removed by ultracentrifugation at 100,000xg for 30 minutes. The supernatant was filtered
454 with a 45 micron filter, supplemented with 20 mM imidazole, and loaded over a gravity Ni-
455 NTA column at 4°C. The column was washed with 10 CV of a buffer containing 250 mM
456 NaCl, 50 mM Tris pH 7.5, 10 mM imidazole, and then eluted with buffer containing 250
457 mM imidazole. Nanobody was concentrated and applied to size exclusion
458 chromatography with a buffer containing 250 mM NaCl and 50 mM Tris pH 7.5.
459 Monomeric fractions were pooled, concentrated, supplemented with 10% glycerol, and
460 snap frozen in liquid nitrogen for later use. Expression and purification of Mb6 and Nb6M
461 was performed identically to Nb6.
462
463 **Expression and Purification of NabFab**
464 Chemically competent C43 *E. coli* were transformed via heat shock with NabFab
465 plasmid[8]. A culture of 10 mL 2xYT media (16g/L tryptone, 10g/L yeast extract, 5g/L NaCl)
466 was inoculated with a single colony and incubated at 37°C with shaking overnight. TB

467 autoinduction media (Terrific Broth supplemented with 0.4% glycerol, 0.01% glucose,
468 0.02% lactose,1.25 mM $MgSO_4$, and 100 μg/ml ampicillin) was inoculated from starter
469 cultures and incubated for 6 hrs at 37 ^oC, 225 rpm, before decreasing the temperature to
470 30^oC for overnight growth. The cells expressing NabFab were harvested by centrifugation
471 and snap-frozen in liquid nitrogen for storage. To purify NabFab, cell pellets were thawed
472 and resuspended in lysis buffer containing 20 mM sodium phosphate, pH 7.4, 150 mM
473 NaCl, DNaseI, and protease inhibitor cocktail), and lysed by sonication. The lysate was
474 then incubated at 63-65 ^oC for 30 minutes before centrifugation at 20,000 xg for 30
475 minutes. The supernatant was collected and run over a Protein G column pre-equilibrated
476 with 20 mM sodium phosphate, 500 mM NaCl, pH 7.4. The NabFab was then eluted with
477 0.1 M acetic acid and immediately loaded onto a Resource S cation exchange column
478 pre-equilibrated with buffer A (50 mM sodium acetate, pH 5.0). The column was washed
479 with 5 CV of buffer A and protein then eluted over a salt gradient 0-100% buffer B (50 mM
480 sodium acetate, 2M NaCl, pH 5.0). Eluted NabFab was dialyzed overnight into 150 mM
481 NaCl, 20 mM HEPES, pH 7.5 and then concentrated to 3 mg/mL for complexation.
482
483 **Expression and Purification of Receptor/Nb6 Complexes**
484 All receptors were expressed in Sf9 insect cells (Expression Systems) infected at a
485 density of 3-4 million cells/ml. At 48 hours post-infection, cells were collected with
486 centrifugation, washed with phosphate-buffered saline containing 10 μM antagonist
487 (when used), and pellets were snap frozen in liquid nitrogen for purification. A general
488 protocol was used for producing receptor/Nb6 complexes (Fig. S1), with some slight
489 deviations. Sf9 pellets containing receptor were lysed in hypotonic buffer containing 20

490 mM HEPES pH 7.5, 5 mM $MgCl_2$, protease inhibitor cocktail, benzonase, 10 μM
491 antagonist (when used), and 2 mg/ml iodoacetamide and gently stirred for an hour at 4°C.
492 Membranes were harvested with ultracentrifugation at 100,000xg, supernatant was
493 discarded, and membranes were resuspended in solubilization buffer containing 250 mM
494 NaCl, 20 mM HEPES pH 7.5, 1 mM $MgCl_2$, protease inhibitor cocktail, 10 μM antagonist
495 (when used), and 2 mg/ml iodoacetamide; then drip frozen into liquid nitrogen and stored
496 at -80°C. Resuspended membranes were thawed and detergent was added dropwise
497 while stirring at 4°C to a final concentration of 1% LMNG/0.1% CHS/0.1% Cholate. After
498 3 hours, insoluble debris was removed with ultracentrifugation at 100,000 g. Solubilized
499 receptor was supplemented with 20 mM imidazole and gravity loaded over a Ni-NTA resin
500 column. Columns were washed with 10 column volumes of buffer containing 250 mM
501 NaCl, 20 mM HEPES pH 7.5, 10 μM antagonist (when used), 20 mM imidazole, and 0.1%
502 LMNG/0.01% CHS and protein was eluted in buffer containing 250 mM NaCl, 20 mM
503 HEPES pH 7.5, 10 μM antagonist (when used), 250 mM imidazole, and 0.01%
504 LMNG/0.001% CHS. Receptor was then supplemented with 5 mM $CaCl_2$ and loaded onto
505 M1 flag resin; washed with 5 column volumes of 250 mM NaCl, 20 mM HEPES pH 7.5,
506 10 μM antagonist (when used), 2 mM CaCl2, and 0.1% LMNG/0.01% CHS; and eluted
507 with buffer containing 150 mM NaCl, 20 mM HEPES pH 7.5, 10 μM antagonist (when
508 used), 1 mM EDTA, 0.2 mg/ml FLAG peptide, and 0.1% LMNG/0.01% CHS. Purified
509 receptor was incubated on ice overnight with HRV 3C protease and purified Nb6 was
510 added at a 2:1 molar ratio. Receptor/Nb6 complex was concentrated in a 50 kDa
511 molecular weight cutoff spin concentrator and subjected to SEC chromatography with an
512 ENrich 650 column (Bio-Rad) and a buffer containing 150 mM NaCl, 20 mM HEPES pH

513 7.5, 0.001% LMNG, 0.00033% GDN, and 0.0001% CHS. Fractions containing monomeric
514 receptor/Nb6 complex were pooled for cryo-EM sample preparation. This protocol was
515 identical for SSTR2, NTSR1, and H2R with the exception of the addition of 100 μM TCEP
516 to the lysis buffer for NTSR1 and incubation with Nb6M, NabFab, and anti-Fab Nb
517 (Thermo Fisher Scientific 1033270500) in the case of H2R. Preparation of MOR/Mb6
518 complex was identical to that of receptor Nb6 complex, with the omission of the HRV-3C
519 cleavage to remove eGFP as it was not present in the construct.
520

521 **Cryo-EM Sample Preparation**

522 All samples were prepared on glow-discharged holey gold grids (Quantifoil ultrAufoil
523 R1.2/1.3), blotted in a FEI Vitrobot Mark IV (Thermo Fisher Scientific) at 4°C and 100%
524 humidity, and plunge frozen into liquid ethane. Blotting conditions for each sample were
525 as follows: 3.0 μl of NTSR1/Nb6 complex at 16 mg/ml with an additional 0.05% beta OG;
526 3.0 μl of MOR/Mb6 complex at 5 mg/ml; 2.5 μl of SSTR2/Nb6 complex at 16 mg/ml with
527 an additional 0.05% beta OG; and 3.0 μl of H2R/Nb6M/NabFab/anti-Fab Nb at 2.5-4
528 mg/ml.
529

530 **Cryo-EM Data Collection**

531 All samples were collected on a KRIOS electron microscope at an accelerating voltage
532 of 300 kV, with an energy filter for NTSR1/Nb6, H2R/Nb6M/NabFab/anti-Fab Nb, and
533 MOR/Mb6 and without an energy filter for SSTR2/Nb6. All data was collected through
534 SerialEM with beam tilt compensation and recorded on a Gatan K3 direct electron
535 detector. The resulting image stacks have a pixel size of 0.434 Å for NTSR1/Nb6,

536 H2R/Nb6/NabFab, MOR/Mb6, and H2R/Nb6M/NabFab/anti-Fab Nb; and 0.426 Å for
537 SSTR2/Nb6, all in super resolution mode. Each NTSR1/Nb6 image stack is composed of
538 71 frames with an incident electron dose of 0.85 $e^-/Å^2$ per frame, for a total dose of 61 e^-
539 $/Å^2/s$ per micrograph. Each MOR/Mb6 image stack is composed of 63 frames with an
540 incident electron dose of 0.98 $e^-/Å^2$ per frame, for a total dose of 61 $e^-/Å^2/s$ per micrograph.
541 Each SSTR2/Nb6 image stack is composed of 55 frames with an incident electron dose
542 of 1.26 $e^-/Å^2$ per frame, for a total dose of 69 $e^-/Å^2/s$ per micrograph. Each
543 H2R/Nb6M/NabFab/anti-Fab Nb image stack is composed of 68 frames with an incident
544 electron dose of 0.86 $e^-/Å^2$ per frame, for a total dose of 58.58 $e^-/Å^2/s$ per micrograph.
545

546 **Cryo-EM Data Processing**

547 A pictorial depiction of each cryoEM processing workflow can be found in Figs. S2C, S4C,
548 S6C, and S8C. Briefly, dose-fractionated image stacks were imported into RELION-3.1[37]
549 and subjected to beam-induced motion correction and dose weighting with MotionCor2[38].
550 Contrast transfer function parameter estimation was performed with CTFFIND-4.1[39].
551 Particle selection and extraction was performed with the Laplacian autopicker function of
552 RELION-3.1 on micrographs with a CTF fit better than 3.5 Å. The extracted particle stack
553 was imported into CryoSPARC[40] and subjected to multiple rounds of 2D classification
554 followed by iterative rounds of *ab initio* reconstruction with multiple classes and
555 heterogeneous refinement to further classify particles. In early 3D iterations, particles
556 from poor 3D classes were subjected to additional 2D classification and good particles
557 were 'rescued' for further 3D classification. Once iterative *ab initio* and heterogenous
558 refinement no longer produced higher resolution reconstruction, particles were re-

559 imported to RELION-3.1. In the cases of hNTSR1 and MOR CTF fit cutoffs of 3.1 Å and
560 3.3 Å were applied, respectively. Particles were then subjected to 3D refinement in
561 RELION-3.1 followed by Bayesian polishing. Polished particles were then imported back
562 to CryoSPARC for non-uniform refinement, global CTF refinement based on optics group,
563 and repeated non-uniform and local refinement.
564

565 **Model Building and Refinement**

566 All initial models were rigid body fit into cryo-EM maps using the ChimeraX[41] software.
567 For hNTSR1, the cryo-EM model of active state hNTSR1 was used as the initial model
568 (PDB:6OS9[19]); for MOR the crystal structure of inactive MOR bound to a covalent
569 antagonist was used as the initial model (PDB:4DKL[42]), for SSTR2 a homology model
570 generated from KOR (PDB:6VI4[4]) was used; and for H2R a homology model generated
571 from H1R (PDB:3RZE[33]) was used. In all cases KOR/Nb6 complex (PDB:6VI4[4]) was
572 aligned to the receptor to produce the initial model for the nanobody. An initial structure
573 for the NabFab was taken from PDB:7PHP. All structures were manually refined in
574 COOT[43] with iterative real-space refinement in Phenix[44]. Once accurate modeling was
575 achieved for the protein components, the GemSpot pipeline[45] was used for automatic
576 modeling of the ligands alvimopan, SR48692, and famotidine into MOR, hNTSR1, and
577 H2R, respectively. Final refinement was executed in Phenix, followed by model-free
578 Phenix map modification for NTSR1 and MOR[46]. All maps displayed in this work are those
579 prior to model-free map modification unless stated otherwise.
580

581 **Molecular Dynamics Simulations**

582 Simulations of the KOR/Nb6 complex started with the crystal structure PDB:6VI4, with the
583 pose of JDTic replaced with that of PDB:4DJH[21]. Maestro's protein preparation tool was
584 used to assign protonation states, optimize hydrogen bonding, and build missing
585 sidechains and loops. Once the receptor was prepared, the orientation of proteins in
586 membranes webserver (OPM)[47] was used to align the receptor as it would be in a
587 membrane in the xy plane and the CHARMM-GUI[48] was used to build the full system with
588 a 1-palmitoyl-2-oleoyl-*sn*-glycero-3-phosphocholine POPC/CHS lipid bilayer, TIP3P
589 water[49], and 150 mM NaCl. PSF and PDB files were generated with the OPLS-AA/M[50,51]
590 forcefield in VMD[52] for the system. For Mb6, a homology model was built from PDB:6XVI
591 with the Prime homology modeling tool[53]. This model was solvated in TIP3P water and
592 150 mM NaCl in VMD for simulation.

593 Molecular dynamics simulations were carried out in NAMD[54] with a 2 fs timestep
594 with SHAKE and SETTLE algorithms[55,56], with a Langevin thermostat and a Nosé-Hoover
595 Langevin piston barostat at 1 atm with a period of 50 fs and decay of 25 fs. Periodic
596 boundary conditions were used with nonbonded interactions smoothed starting at 10 Å to
597 12 Å with long-range interactions treated with particle mesh Ewald (PME). The system
598 was minimized for 1,500 steps and then slowly heated from 0 to 303.15K in increments
599 of 20K simulating for 0.4 ns at each increment. For the Kappa/Nb6 simulations, all non-
600 hydrogen, non-water, and non-ion atoms were restrained with a 1 kcal/mol/ $Å^2$ harmonic
601 restraint during heating and an additional 10 ns of equilibration. 1 kcal/mol/ $Å^2$ harmonic
602 restraints were used for an additional 10 ns of equilibration on all non-hydrogen protein
603 atoms followed by a final 10 ns of restrained equilibration with 1 kcal/mol/ $Å^2$ harmonic
604 restraint on only $C\alpha$ atoms. The first 30 ns of unrestrained molecular dynamics were also

605 considered to be equilibration, with an additional 500 ns of simulation performed. All
606 simulations were performed in triplicate. For Mb6, the first 30 ns of unrestrained molecular
607 dynamics were treated as equilibration, and 100 ns of triplicate molecular dynamics
608 simulations were performed.
609
610 **Docking**
611 The cryo-EM structure of active MOR (PDB:6DDE)[3] was prepared in Maestro and
612 carfentanil was docked with Glide XP docking[57]. The cryo-EM structure of inactive H2R
613 was prepared in Maestro, and ranitidine and cimetidine were docked with Glide XP
614 docking[57]. The crystal structure of inactive H1R (PDB:3RZE) was prepared in Maestro
615 and loratadine and cetirizine were docked with Glide XP docking[57].
616
617 **References**
618 1. Robertson, M. J., Meyerowitz, J. G. & Skiniotis, G. Drug discovery in the era of cryo-
619 electron microscopy. *Trends in Biochemical Sciences* (2021).
620 doi:10.1016/j.tibs.2021.06.008
621 2. Hauser, A. S., Attwood, M. M., Rask-Andersen, M., Schiöth, H. B. & Gloriam, D. E. Trends
622 in GPCR drug discovery: New agents, targets and indications. *Nat. Rev. Drug Discov.*
623 (2017). doi:10.1038/nrd.2017.178
624 3. Koehl, A. *et al.* Structure of the μ-opioid receptor-Gi protein complex. *Nature* **558**, 547–552
625 (2018).
626 4. Che, T. *et al.* Nanobody-enabled monitoring of kappa opioid receptor states. *Nat. Commun.*
627 (2020). doi:10.1038/s41467-020-14889-7
628 5. Gully, D. *et al.* Biochemical and pharmacological profile of a potent and selective
629 nonpeptide antagonist of the neurotensin receptor. *Proc. Natl. Acad. Sci. U. S. A.* (1993).

630 doi:10.1073/pnas.90.1.65

631 6. Uchański, T. *et al.* Megabodies expand the nanobody toolkit for protein structure
632 determination by single-particle cryo-EM. *Nat. Methods* (2021). doi:10.1038/s41592-020-
633 01001-6

634 7. Zimmerman, D. M. *et al.* Discovery of a Potent, Peripherally Selective trans-3,4-Dimethyl-
635 4-(3-hydroxyphenyl)piperidine Opioid Antagonist for the Treatment of Gastrointestinal
636 Motility Disorders. *J. Med. Chem.* (1994). doi:10.1021/jm00041a003

637 8. Bloch, J., Mukherjee, S., Kowal, J., Filippova, E. V., Niederer, M., Pardon, E., Seyaert, J.,
638 Kossiakoff, A. A., Locher, K. P. Development of a universal nanobody-binding Fab module
639 for fiducial-assisted cryo-EM strudies of membrane proteins *P.N.A.S.* (2021)
640 doi:10.1073/pnas.2115435118

641 9. Carraway, R. & Leeman, S. E. Characterization of radioimmunoassayable neurotensin in
642 the rat. Its differential distribution in the central nervous system, small intestine, and
643 stomach. *J. Biol. Chem.* (1976). doi:10.1016/s0021-9258(17)32938-1

644 10. Christou, N. *et al.* Neurotensin pathway in digestive cancers and clinical applications: an
645 overview. *Cell Death and Disease* (2020). doi:10.1038/s41419-020-03245-8

646 11. Liu, J. *et al.* neurotensin receptor 1 antagonist SR48692 improves response to carboplatin
647 by enhancing apoptosis and inhibiting drug efflux in ovarian cancer. *Clin. Cancer Res.*
648 (2017). doi:10.1158/1078-0432.CCR-17-0861

649 12. Volkow, N. D. & Blanco, C. The changing opioid crisis: development, challenges and
650 opportunities. *Molecular Psychiatry* (2021). doi:10.1038/s41380-020-0661-4

651 13. Volkow, N. D. & Collins, F. S. The Role of Science in Addressing the Opioid Crisis. *N. Engl.*
652 *J. Med.* (2017). doi:10.1056/nejmsr1706626

653 14. Günther, T. *et al.* International union of basic and clinical pharmacology. CV. somatostatin
654 receptors: Structure, function, ligands, and new nomenclature. *Pharmacol. Rev.* (2018).
655 doi:10.1124/pr.117.015388

656 15. Ballesteros, J. A. & Weinstein, H. Integrated methods for the construction of three-
657 dimensional models and computational probing of structure-function relations in G protein-
658 coupled receptors. *Methods Neurosci.* (1995). doi:10.1016/S1043-9471(05)80049-7
659 16. Stoeber, M. *et al.* A Genetically Encoded Biosensor Reveals Location Bias of Opioid Drug
660 Action. *Neuron* (2018). doi:10.1016/j.neuron.2018.04.021
661 17. Deluigi, M. *et al.* Complexes of the neurotensin receptor 1 with small-molecule ligands
662 reveal structural determinants of full, partial, and inverse agonism. *Sci. Adv.* (2021).
663 doi:10.1126/sciadv.abe5504
664 18. Mittl, P. R., Ernst, P. & Plückthun, A. Chaperone-assisted structure elucidation with
665 DARPins. *Current Opinion in Structural Biology* (2020). doi:10.1016/j.sbi.2019.12.009
666 19. Scott, D. J., Kummer, L., Egloff, P., Bathgate, R. A. D. & Plückthun, A. Improving the apo-
667 state detergent stability of NTS1 with CHESS for pharmacological and structural studies.
668 *Biochim. Biophys. Acta - Biomembr.* (2014). doi:10.1016/j.bbamem.2014.07.015
669 20. Kato, H. E. *et al.* Conformational transitions of a neurotensin receptor 1–Gi1 complex.
670 *Nature* **572**, 80–85 (2019).
671 21. Russo, C. J. & Passmore, L. A. Ultrastable gold substrates for electron cryomicroscopy.
672 *Science (80-.).* (2014). doi:10.1126/science.1259530
673 22. Wu, H. *et al.* Structure of the human κ-opioid receptor in complex with JDTic. *Nature* (2012).
674 doi:10.1038/nature10939
675 23. Van Bever, W. F. M., Niemegeers, C. J. E. & Schellekens, K. H. L. P. A. J. N 4 substituted
676 1 (2 arylethyl) 4 piperidinyl N phenylpropanamides, a novel series of extremely potent
677 analgesics with unusually high safety margin. *Arzneimittel-Forschung/Drug Res.* (1976).
678 24. Robertson, M. J., Meyerowitz, J. M., Panova, O., Borrelli, K. W., Skiniotis, G. Plasticity in
679 Ligand Recognition at Somatostatin Receptors. *NSMB* (2022)
680 25. Tunyasuvunakool, K. *et al.* Highly accurate protein structure prediction for the human
681 proteome. *Nature* (2021). doi:10.1038/s41586-021-03828-1

682 26. Baek, M. *et al.* Accurate prediction of protein structures and interactions using a three-track
683 neural network. *Science (80-.).* (2021). doi:10.1126/science.abj8754
684 27. Kong, H., Raynor, K., Yasuda, K., Bell, G. I. & Reisine, T. Mutation of an aspartate at
685 residue 89 in somatostatin receptor subtype 2 prevents Na+ regulation of agonist binding
686 but does not alter receptor-G protein association. *Mol. Pharmacol.* (1993).
687 28. Martin, S., Botto, J. M., Vincent, J. P. & Mazella, J. Pivotal role of an aspartate residue in
688 sodium sensitivity and coupling to G proteins of neurotensin receptors. *Mol. Pharmacol.*
689 (1999). doi:10.1124/mol.55.2.210
690 29. Yabaluri, N. & Medzihradsky, F. Regulation of μ-opioid receptor in neural cells by
691 extracellular sodium. *J. Neurochem.* (1997). doi:10.1046/j.1471-4159.1997.68031053.x
692 30. Fenalti, G. DRUG DISCOVERY Molecular control of delta -opioid receptor signalling. *Nat.*
693 *-LONDON-* (2014).
694 31. Ereño-Orbea J., Sicard T., Cui H., Carson J., Hermans P., Julien J.P. Structural Basis of
695 Enhanced Crystallizability Induced by a Molecular Chaperone for Antibody Antigen-Binding
696 Fragments *J. Mol. Biol.* (2018)
697 32. Xu, P. *et al.* Structural insights into the lipid and ligand regulation of serotonin receptors.
698 *Nature* (2021) doi:10.1038/s41586-021-03376-8.
699 33. Shimamura, I., *et al.* Structure of the human histamine H1 receptor complex with doxepin.
700 *Nature* (2011) doi:10.1038/nature10246.
701 34. Marosi, A., Szalay, Z., Béni, S., Szakács, Z., Gáti, T., Rácz, Á., Noszál, B., Demeter, Á.
702 Solution-state NMR spectroscopy of famotidine revisited: spectral assignment, protonation
703 sites, and their structural consequences. *Anal. Bioanal. Chem.* (2021) doi:10.1007/s00216-
704 011-5599-6.
705 35. Gantz, I., DelValle, J., Wang. L-D., Tashiro, T., Munzert, G., Guo, Y-J., Konda, Y., Yamada,
706 Y. Molecular Basis for the Interaction of Histamine with the Histamine H2 Receptor. *J. Biol.*
707 *Chem.* (1992) doi:10.1016/S0021-9258(19)36764-X.

708 36. Towns, J. *et al.* XSEDE: Accelerating scientific discovery. *Comput. Sci. Eng.* (2014).
709 doi:10.1109/MCSE.2014.80
710 37. Zivanov, J. *et al.* RELION-3: New tools for automated high-resolution cryo-EM structure
711 determination. *bioRxiv* (2018). doi:10.1101/421123
712 38. Zheng, S. Q. *et al.* MotionCor2: Anisotropic correction of beam-induced motion for
713 improved cryo-electron microscopy. *Nature Methods* **14**, 331–332 (2017).
714 39. Rohou, A. & Grigorieff, N. CTFFIND4: Fast and accurate defocus estimation from electron
715 micrographs. *J. Struct. Biol.* **192**, 216–221 (2015).
716 40. Punjani, A., Rubinstein, J. L., Fleet, D. J. & Brubaker, M. A. CryoSPARC: Algorithms for
717 rapid unsupervised cryo-EM structure determination. *Nat. Methods* (2017).
718 doi:10.1038/nmeth.4169
719 41. Pettersen, E. F. *et al.* UCSF ChimeraX: Structure visualization for researchers, educators,
720 and developers. *Protein Sci.* (2021). doi:10.1002/pro.3943
721 42. Manglik, A. *et al.* Crystal structure of the μ-opioid receptor bound to a morphinan
722 antagonist. *Nature* (2012). doi:10.1038/nature10954
723 43. Emsley, P., Lohkamp, B., Scott, W. G. & Cowtan, K. Features and development of Coot.
724 *Acta Crystallogr. Sect. D Biol. Crystallogr.* **66**, 486–501 (2010).
725 44. Adams, P. D. *et al.* PHENIX: A comprehensive Python-based system for macromolecular
726 structure solution. *Acta Crystallogr. Sect. D Biol. Crystallogr.* **66**, 213–221 (2010).
727 45. Robertson, M. J., van Zundert, G. C. P., Borrelli, K. & Skiniotis, G. GemSpot: A Pipeline for
728 Robust Modeling of Ligands into Cryo-EM Maps. *Structure* (2020).
729 doi:10.1016/j.str.2020.04.018
730 46. Terwilliger, T. C., Ludtke, S. J., Read, R. J., Adams, P. D. & Afonine, P. V. Improvement of
731 cryo-EM maps by density modification. *Nat. Methods* (2020). doi:10.1038/s41592-020-
732 0914-9
733 47. Lomize, M. A., Pogozheva, I. D., Joo, H., Mosberg, H. I. & Lomize, A. L. OPM database

734 and PPM web server: Resources for positioning of proteins in membranes. *Nucleic Acids*
735 *Res.* **40**, (2012).
736 48. Lee, J. *et al.* CHARMM-GUI Input Generator for NAMD, GROMACS, AMBER, OpenMM,
737 and CHARMM/OpenMM Simulations Using the CHARMM36 Additive Force Field. *J.*
738 *Chem. Theory Comput.* **12**, 405–413 (2016).
739 49. Jorgensen, W. L., Chandrasekhar, J., Madura, J. D., Impey, R. W. & Klein, M. L.
740 Comparison of simple potential functions for simulating liquid water. *J. Chem. Phys.* **79**,
741 926–935 (1983).
742 50. Robertson, M. J., Tirado-Rives, J. & Jorgensen, W. L. Improved Peptide and Protein
743 Torsional Energetics with the OPLS-AA Force Field. *J. Chem. Theory Comput.* **11**, 3499–
744 3509 (2015).
745 51. Robertson, M. J., Skiniotis, G. Development of OPLS-AA/M Parameters for Simulations of
746 G-Protein Coupled Receptors and other Membrane Proteins. *bioRxiv.* (2022).
747 52. Humphrey, W., Dalke, A. & Schulten, K. VMD: Visual molecular dynamics. *J. Mol. Graph.*
748 **14**, 33–38 (1996).
749 53. Jacobson, M. P. *et al.* A Hierarchical Approach to All-Atom Protein Loop Prediction.
750 *Proteins Struct. Funct. Genet.* (2004). doi:10.1002/prot.10613
751 54. Phillips, J. C. *et al.* Scalable molecular dynamics with NAMD. *Journal of Computational*
752 *Chemistry* **26**, 1781–1802 (2005).
753 55. Ryckaert, J. P., Ciccotti, G. & Berendsen, H. J. C. Numerical integration of the cartesian
754 equations of motion of a system with constraints: molecular dynamics of n-alkanes. *J.*
755 *Comput. Phys.* (1977). doi:10.1016/0021-9991(77)90098-5
756 56. Miyamoto, S. & Kollman, P. A. Settle: An analytical version of the SHAKE and RATTLE
757 algorithm for rigid water models. *J. Comput. Chem.* (1992). doi:10.1002/jcc.540130805
758 57. Friesner, R. A. *et al.* Extra precision glide: Docking and scoring incorporating a model of
759 hydrophobic enclosure for protein-ligand complexes. *J. Med. Chem.* **49**, 6177–6196

760 (2006).

761